Probabilistic Inverse Problem to Characterize Tissue-Equivalent Material Mechanical Properties

Nicolas Bochud and Guillermo Rus

Abstract—The understanding of internal processes that affect the changes of consistency of soft tissue is a challenging problem. An ultrasound-monitoring Petri dish has been designed to monitor the evolution of relevant mechanical parameters during engineered tissue formation processes in real time. A better understanding of the measured ultrasonic signals required the use of numerical models of the ultrasound–tissue interactions. The extraction of relevant data and its evolution with sufficient sensitivity and accuracy is addressed by applying well-known signal processing techniques to both the experimental and numerically predicted measurements. In addition, a stochastic model-class selection formulation is used to rank which of the proposed interaction models are more plausible. The sensitivity of the system is verified by monitoring a gelation process.

I. Introduction

THE rational principles of continuum mechanics are proposed, together with a formal signal processing framework, to address the problem of characterizing mechanical properties of tissue cultures based on noninvasive and nonionizing ultrasonic measurements.

The objectives of this study are to design an ultrasound-monitoring Petri dish and to monitor in real time the evolution of relevant mechanical parameters during engineered tissue formation processes. Many types of uncertainties involved in the modeling of interaction between ultrasonic waves and tissue, such as excitation, material viscosity, and material heterogeneity are responsible for noise in the output. In this paper, several models of ultrasound–tissue interaction are proposed, implemented, and contrasted against experimental observations. All assume homogeneous media with varying moduli and energy-dissipation forms that are expressed as attenuation models. High-frequency ultrasound is adopted for excitation and measurement to analyze and interact with small-scale specimens. The minimization between experimental and numerically predicted measurements is addressed by solving a probabilistic inverse problem which includes advanced signal processing techniques.

In the nondestructive evaluation (NDE) community, signal processing techniques have played an increasing role in recent decades [1]. An essential element in NDE systems is the analysis of the captured signal, by means of a noise-free parameter extraction, to obtain relevant information from the tested specimen. Among the methods of noise impact minimization, it is worth noting filtering techniques: Rodríguez *et al.* [2] selected the frequency range corresponding to the detected echoes location. Thus, by making use of the Wigner-Ville transform, the echoes from the crack can be distinguished from the noisy echoes generated by the scattered ultrasonic waves through the material grains. Bilgutay *et al.* [3] proposed a transformation based on filter-bank techniques by applying the split spectrum processing (SSP) method to obtain a reconstructed signal less affected by noise.

The first proposals to solve the deconvolution problem in NDE use classical techniques, such as the Wiener filter, spectral extrapolation, deconvolution of minimal least variance, estimation of the least squares [4], or homomorphic deconvolution by computation of the cepstrum [5]. The cepstrum also has been used as an efficient parameterization tool for ultrasonics signals, because the cepstral coefficients involve deconvoluted signal information [6]. Higher-order statistics (HOS) enables the developing of blind deconvolution techniques, avoiding any prior information on the signal noise or defect [7]. In some cases, the extracted signal parameters can be processed again to reduce the dimensionality of the feature vectors, by applying classical linear discriminant analysis (LDA) [8] or principal components analysis (PCA) [9].

Recently, signal processing methods have been increasingly used to provide suitable features extraction from biomedical imaging, especially for elastography imaging (B-scan), to diagnose pathologies. Ultrasound data were captured from postmortem coronary arteries to develop RF analysis techniques for the characterization of atherosclerotic plaque [10]. A system was proposed by Scheipers *et al.* [11] for prostate diagnostics based on multifeature tissue characterization. Their neuro-fuzzy inference system combines spectral features and textural features of first and second order with clinical variables and morphological descriptors for disease classification. Abeyratne and Tang [12] proposed the use of a wavelet-transform-based technique to estimate the interscatterer distribution (ISS) in diagnosing focal diseases of the liver. Maggio *et al.* [13] employed a multi-feature kernel classification model based on generalized discriminant analysis to support

prostate cancer diagnosis. Siebers *et al.* [14] presented an ultrasound based system for computer-aided characterization of biological tissue and its application to differential diagnosis of parotid gland lesions, based on a supervised classification of malignant and benign cases using tissue-describing features derived from ultrasound RF echo signals and image data.

However, most of the aforementioned applications deal with determination of the presence of damages/pathologies in the evaluated specimen. Hence, the final goal of the system is limited to a classification of the states damage/no damage or malignant/benign, respectively. These techniques require a huge amount of experimental data and an expensive training process, without providing any information at the physical level or using knowledge about the physiology to aid the decision.

Linear ultrasound techniques have been widely used to quantify the elastic properties of tissue, and thus to differentiate between normal and diseased tissue. One way to measure elastic modulus is quasi-static elastography [15]–[17], in which the displacement is induced by indentation and the strain is computed by a speckle-tracing method. The resulting shear wave displacement propagation can be ultrasonically tracked through time and the elastic modulus of the tested medium calculated. A commercial device following the concept by Bercoff *et al.* [18] was commercialized by Supersonic Imagine as an extended echographic device. The impulsive force excitation combined with ultrasound vibrometry developed by Sandrin *et al.* [19] has been commercialized by Echosens under the name of Fibroscan as a liver disorder diagnosis device. Other authors have proposed several laboratory-scale imaging modalities that provide information about shear elastic properties of tissue. Shear waves can be generated within tissues using focused, impulsive, acoustic radiation force excitations [20]–[22], acoustic remote palpation, sonoelastography, or shear wave dispersion ultrasound vibrometry. Shear and compressional moduli of quasi-incompressible materials, such as tissue, are a consequence of different micro-mechanisms, and therefore have the potential to highlight related but different aspects of the physicochemical properties of the tissue.

Some recent experimental observation may tangentially suggest that nonlinear mechanical properties may be a key signature to quantify tissue consistency changes, even better than just bulk or shear moduli. Barannik *et al.* [23] revealed the mechanical relaxation processes appearing at higher frequencies than in the quasi-static regime. The appearance of these relaxation dynamics was associated with the presence of inhomogeneities in tissue. In recent years, numerous models have been developed in the NDE community that investigate the possibility of using non-linear techniques to detect damaged interfaces in solids [24], [25] or dynamic nonlinear stress–strain features in micro-inhomogeneous materials [26]–[28]. Recently, some authors have extended some of these experimental techniques (NRUS, NEWS, etc.) for application to damage

assessment in cortical bone [29] and to measure acoustic nonlinearity in trabecular bone [30].

Despite the widespread use of experimental techniques, only a few works have dealt with the model-based reconstruction of the elastic properties of soft tissue. Among them, Moulton *et al.* [31] solved an inverse boundary value problem to determine the unknown material parameters for a nonlinear, nonhomogeneous material law, using a *p*-version finite element model of the heart. Han *et al.* [32] presented a finite-element-based nonlinear inverse scheme to reconstruct the elastic properties of soft tissues subjected to an external compression. Recently, Guo *et al.* [33] developed a novel finite element method-based direct method for the material reconstruction in soft tissue elastography.

The proposed system avoids the need of steps such as cross-correlation of echographic images, by a more direct procedure, hence increasing the precision. It also allows the use of a complex propagation model to quantify model parameters of interest beyond modulus and attenuation. Nonlinear phenomena have not been considered in this study, but this is a research topic currently under development at our laboratory. This void in the mechanical characterization and interpretation of material defects may be overcome by adopting model-based inverse problem strategies. This is the main goal of the present work, which is successfully applied for tissue characterization. This approach allows one to obtain not only the optimal parameters in a model class, but also the uncertainty associated with the parameter estimates. Some recent developments and civil engineering applications of Bayesian model class selection have been carefully reviewed by Yuen [34]. The model-class selection is formulated following Beck and Yuen [35]. Finally, a simple formulation of the joint probability is proposed, from which either the inverse problem or the model-class selection can be derived just by extracting specific marginal probabilities, thus unifying all of the approaches.

A model-class selection algorithm is useful to understand unknown propagation models in complex materials such as engineered tissue, which is the specimen this device will be used for. With the purpose of validating the model-class selection algorithm, a gelation process is monitored and analyzed, the behavior of which is controlled and assumed by the majority of the literature to be viscoelastic [36]–[38].

II. Methodology

The proposed methodology combines four elements. 1) The signal acquisition of the ultrasonic signals obtained from the waves' interaction with a sample of tissue; 2) a set of alternative attenuation models that simulate the ultrasound–tissue interaction, which is numerically solved by the transfer matrix formalism; 3) a stochastic model-class selection formulation used to rank which of the

TABLE I. Mechanical Properties of Materials.

Material	Modulus [Pa]	Poisson's ratio ν	Density ρ [kg/m^3]	Speed c_p [m/s]
PMMA	$E = 2960 \cdot 10^6$	0.43	1180	2673
Gel (initial)	Unknown	0.5	1000	Unknown

models parameterization are more plausible; and 4) an NDE-oriented signal processing framework that extracts relevant features from both the experimental and numerically predicted signals. The latter is used to reconstruct the evolution of the relevant mechanical parameters during the culture reaction time.

A. Experimental Setup

A Petri dish with a specifically designed high-frequency ultrasonic transmitter and receiver in an angled position was manufactured for real-time measurement of mechanical and geometrical properties of thin layers of tissue culture (of the order of 100 µm). The monitored Petri dish is connected to the electronic setup detailed in Fig. 1.

The transmitting and receiving transducers are designed to be in an angled position (45°) to avoid reverberation echoes inside the parts of the Petri dish plate. The transmitted signal is generated as a 1-cycle burst composed by a 20-MHz sine of amplitude that amounts to 5 V with a repetition rate of 1000 pulses/s, using an arbitrary wave generator (33220, Agilent Technologies Inc., Santa Clara, CA). The recording is digitized with a high resolution A/D converter after 40 dB preamplification, for a period of 5 µs with a sampling rate of 400 MHz. The gelation process is monitored for half an hour at 5-s intervals, resulting in a database of 350 measurements. Each measurement corresponds to the average of 300 captures of the signal, providing an effective reduction of noise according to the signal-to-noise ratio (25 dB). Only compressional waves are generated by the transducers and no mode conversion waves are measured in the present case, although the methodology is extensible to shear or other waves.

The materials and the concentration for the gel culture were chosen according to Ortega et al. [39]: 92.5% water,

5% glycerol, and 2.5% agar. To obtain a homogeneous solution, water was first heated and then the remaining components were added. The final mixture was carefully deposited on the dish, resulting in a gel layer of about 300 µm thickness, and a diameter of 2 cm. At the start of the process, the wave velocity in the gel layer is unknown. Nonetheless, it is well-known that its value is approximately 1500 m/s, and thus the resulting wavelength (75 µm) is compatible with the gel layer thickness. The material properties of the Petri dish material [poly(methyl methacrylate) (PMMA)] and the gel culture are summarized in Table I.

B. Propagation Models

The experimental system is idealized by a mathematical model of the propagation and interaction of the transmitted ultrasonic waves with all the parts of the system until they are received by the sensor. The relevant ultrasonic paths along the Petri dish material (PMMA) and the gel culture are illustrated in Fig. 1.

Several models are tested to idealize the removal of energy by dissipation or radiation. Three alternative damping models are used: 1) viscous, 2) hysteretic, and 3) proportional to integer time derivatives of the particle movement, based on their fractional time derivatives. The damping is defined in terms of the wave modulus M, which is modified from the undamped modulus M_0 to generate a dispersive one, which is a frequency-dependent complex modulus $M^*(\omega)$, where ω is the angular frequency if the modulus dispersion is represented by its frequency domain. The viscous model is defined in terms of the frequency-dependent loss factor η, obtained as the ratio between loss and storage moduli [40]. In this context, a specific view of hysteretic damping is taken, in which it is expressed as
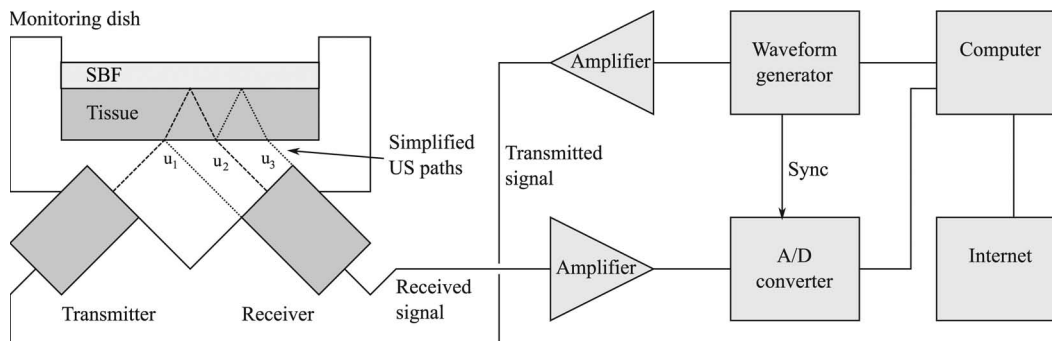

Fig. 1. Schematic diagram of experimental and electronic setup.

a frequency-independent damping [41]. The last model, based on fractional time derivatives, leads to a damping function that may be expressed as a power law, and thus improves curve-fitting properties for relaxation [40], [41]. These models are selected according to their performance demonstrated in a previous study [42]. The viscoelastic η and hysteretic ζ models are defined according to Maia *et al.* [43],

$$M^*(\omega) = M^0(1 - i\omega\eta) \tag{1}$$

and

$$M^*(\omega) = M^0(1 - i\zeta), \tag{2}$$

where η and ζ are the viscoelastic and hysteretic damping coefficients of tissue, respectively. The fractional time derivative damping is defined as

$$M^*(\omega) = M^0 \frac{1 + b(i\omega)^\beta}{1 + a(i\omega)^\alpha}. \tag{3}$$

The three models are summarized in Table II, highlighting the combination of the considered parameters, where K^{tissue} denotes the bulk modulus of tissue. The fractional derivative constants are defined as a, b, and $\alpha = \beta$. Two additional parameters z^{ampl} and z^{time} are introduced to control the correction of the amplitude and the time-shift of the input signal in the culture, which correct effects of temperature and other phenomena on the sensors that affect attenuation and delay on the path from the electronics to the arrival of the signal at the culture specimen. The input signal $s^0(t)$ correction is defined as

$$s^*(t) = z^{\text{ampl}} s^0(t + z^{\text{time}}). \tag{4}$$

The factor z^{ampl} corrects variations of the amplitude and phase of the excitation over the reaction process time that may be influenced by several simultaneous factors, including the temperature. Nonetheless, we assume that these factors can be summarized as a whole by introducing a phenomenological factor, labeled as z^{time}.

The mathematical model is approximated by a semi-analytical model of the wave interactions within multilayered materials based on the transfer matrix formalism (TMF) [44], describing the ultrasonic waves' interactions between the Petri dish and the culture.

C. Probabilistic Inverse Problem

Reconstructing the values of the model parameters (moduli, attenuation parameters, etc.) has a limited meaning if one considers the existence of intrinsic noise

in the measurements, heterogeneity of properties within the specimen, and even the fact that the model used to idealize its behavior is just an approximation of reality. To provide a suitable answer, probabilistic, rather than deterministic, values should be provided, which carry information about the degree of uncertainty and the nature of their scattering. This is solved by treating the input and known data as uncertain and therefore probabilistic, and consequently obtaining the solution model in terms of a set of probability density functions (PDF) over each model parameter as a combination of their degree of certainty provided by the measurements on one hand and the model on the other.

Following the probabilistic formulation of the model reconstruction inverse problem established by Tarantola [45], the solution is not a single-valued set of model parameters $\mathcal{M}$. On the contrary, the solution is provided by probability density functions (PDF) $p(\mathcal{M})$ of the values of the model parameters $\mathcal{M}$ within the manifold $\mathfrak{M}$ of possible values. The probability density p is assigned the meaning of the plausibility of the model values $\mathcal{M}$ being true. The theory of evidential probability concerns the impact of evidence on physical probability. It is motivated by two basic ideas [46]: probability assessments should be based upon relative frequencies, to the extent that we know them, and the assignment of probability to specific individual events should be determined by everything that is known about that individual event. In particular, the probability of a hypothesis H is given the sense of degree of support (or plausibility or belief) of H given empirical evidence.

In this paper, this formulation is generalized to the case in which several model classes $\mathcal{C}$ are candidates to idealize the real excitation-observation. Including this variable into the inverse problem formulation will allow derivation of the model-class selection formulation as a particular case of inverse problem.

Because an absolute probability cannot be computed, statistical inference theory is used to incorporate the *a priori* information about the measured observations $\mathcal{O}$, the model parameters $\mathcal{M}$, and the model class $\mathcal{C}$, and the information of the idealized relationship between them $\mathcal{O} = \mathcal{O}(\mathcal{M})$ is computed by a numerical model pertaining to a model class $\mathcal{C}$. They are defined by the probability densities to prior (labeled with a superscript 0) data $p^0(\mathcal{O})$, $p^0(\mathcal{M})$, and $p^0(\mathcal{C})$, respectively, whereas the additional information about relationship (labeled with a superscript m) between observations and model provided by the model class $\mathcal{C}$ is given by the PDF $p^{\text{m}}(\mathcal{O}, \mathcal{M} \mid \mathcal{C})$. The *a posteriori* probability $p(\mathcal{O}, \mathcal{M}, \mathcal{C})$ of the hypothetical model $\mathcal{M}$ is obtained jointly with the observations $\mathcal{O}$ and class $\mathcal{C}$, as

$$p(\mathcal{O}, \mathcal{M}, \mathcal{C}) = k_1 \frac{p^0(\mathcal{O}, \mathcal{M}, \mathcal{C}) p^{\text{m}}(\mathcal{O}, \mathcal{M}, \mathcal{C})}{\mu(\mathcal{O}, \mathcal{M}, \mathcal{C})}, \tag{5}$$

where $\mu(\mathcal{O}, \mathcal{M}, \mathcal{C})$ is the noninformative density function and k_1 is a normalization constant. Some assumptions will

TABLE II. COMBINATION OF MODELS.

Tag	Size	Parameters					
1	4	K^{tissue}	ζ	z^{ampl}	z^{time}		
2	4	K^{tissue}	η	z^{ampl}	z^{time}		
3	6	K^{tissue}	a	b	$\alpha = \beta$	z^{ampl}	z^{time}

be made at this point. Assuming first that $\mathcal{O}$, $\mathcal{M}$, and $\mathcal{C}$ are independent *a priori* allows splitting of the joint prior information $p^0(\mathcal{O}, \mathcal{M}, \mathcal{C}) = p^0(\mathcal{O})p^0(\mathcal{M})p^0(\mathcal{C})$ and the uniform distribution $\mu(\mathcal{O}, \mathcal{M}, \mathcal{C}) = \mu(\mathcal{O})\mu(\mathcal{M})\mu(\mathcal{C})$. Second, the probabilistic model can be represented by a computation of $\mathcal{O}$ depending on $\mathcal{M}$, which yields $p^{\mathrm{m}}(\mathcal{O}, \mathcal{M}, \mathcal{C}) = p^{\mathrm{m}}(\mathcal{O} \mid \mathcal{M}, \mathcal{C})p^{\mathrm{m}}(\mathcal{M}, \mathcal{C})p^{\mathrm{m}}(\mathcal{C})$. Third, the model is not assumed to provide conditional information between model and class, i.e., $p^{\mathrm{m}}(\mathcal{M}, \mathcal{C}) = \mu(\mathcal{M})$, $p^{\mathrm{m}}(\mathcal{C}) = \mu(\mathcal{C})$, are noninformative. This simplifies the expression to

$$p(\mathcal{O}, \mathcal{M}, \mathcal{C}) = k_1 \frac{p^0(\mathcal{O})p^0(\mathcal{M})p^0(\mathcal{C})p^{\mathrm{m}}(\mathcal{O} \mid \mathcal{M}, \mathcal{C})}{\mu(\mathcal{O})}. \quad (6)$$

The posterior probability of the model $\mathcal{M}$ is obtained from the joint probability $p(\mathcal{O}, \mathcal{M}, \mathcal{C})$ by extracting the marginal probability $p(\mathcal{M})|_{\mathcal{C}=\mathcal{C}_i}$ for all possible observations $\mathcal{O} \in \mathfrak{O} \Rightarrow p^0(\mathcal{C} = \mathcal{C}_i) = 1$, given that the model class $\mathcal{C}_i \in \mathfrak{C}$ is assumed to be true,

$$\begin{aligned} p(\mathcal{M})|_{\mathcal{C}=\mathcal{C}_i} &= \int_{\mathcal{C}=\mathcal{C}_i}\int_{\mathfrak{O}} p(\mathcal{O}, \mathcal{M}, \mathcal{C})\mathrm{d}\mathcal{O}\mathrm{d}\mathcal{C} \\ &= k_2 \int_{\mathfrak{O}} \frac{p^0(\mathcal{O})p^0(\mathcal{M})p^{\mathrm{m}}(\mathcal{O} \mid \mathcal{M}, \mathcal{C})}{\mu(\mathcal{O})}\mathrm{d}\mathcal{O}. \end{aligned} \quad (7)$$

As a fourth simplification, we assume no prior information about the model $p^0(\mathcal{M})$, which is therefore represented by the noninformative distribution $p^0(\mathcal{M}) = \mu(\mathcal{M})$, which can in turn be dropped in the case that Jeffreys parameters are adopted,

$$p(\mathcal{M})|_{\mathcal{C}=\mathcal{C}_i} = k_3 \int_{\mathfrak{O}} p^0(\mathcal{O})p^{\mathrm{m}}(\mathcal{O} \mid \mathcal{M}, \mathcal{C})\mathrm{d}\mathcal{O}, \quad (8)$$

where k_3 is a normalization constant that replaces the dropped uniform distributions, and is needed for $p(\mathcal{M})|_{\mathcal{C}=\mathcal{C}_i}$ to fulfill the theorem of total probability $\int_{\mathfrak{M}} p(\mathcal{M})|_{\mathcal{C}=\mathcal{C}_i} \mathrm{d}\mathcal{M} = 1$.

Fifth, the observations are assumed to follow a Gaussian distribution $\mathcal{O} \sim \mathcal{N}(E[\mathcal{O}^{\mathrm{exp}}], C^{\mathrm{exp}})$ with a mean that is the mean of the experimental observations $\mathcal{O}^{\mathrm{exp}}$, and a covariance matrix C^{exp} that stands for the measurement noise. Sixth and last, the observations are assumed to be a Gaussian process $\mathcal{O} \sim \mathcal{N}(\mathcal{O}(\mathcal{M}), C^{\mathrm{num}})$ centered at the numerically computed ones $E[\mathcal{O}^{\mathrm{num}}] = \mathcal{O}(\mathcal{M})$ with covariance matrix C^{num}.

The probabilistic observations $\mathcal{O}$ are, in our case, a vector of functions of time $\mathcal{O} = o_i(t)$ at every measuring time $t \in [0, T]$ and repetition $i \in [1 \ldots N_i]$, and the aforementioned assumptions are valid for every instant t and sensor i. Considering that the compound probability of the information from all sensors and time instants is the product of that of each one individually, and that this product is equivalent to a summation within the exponentiation (because an integration along the continuous time can be

seen as a summation over every infinitesimal $\mathrm{d}t$), the Gaussian distribution allows for an explicit expression of the probability densities,

$$J(\mathcal{M}) = \frac{1}{2}\sum_{i,j=1}^{N_i}\int_{t=0}^{T} O_i(c_{ij}^{\mathrm{exp}} + c_{ij}^{\mathrm{num}})^{-1}O_j\mathrm{d}t, \quad (9)$$

where $O_k = (o_k(t, \mathcal{M}) - o_k^{\mathrm{exp}}(t))$, $\forall k = i, j$. The term $J(\mathcal{M})$ corresponds to a misfit function between model and observations,

$$p(\mathcal{M})|_{\mathcal{C}=\mathcal{C}_i} = k_4 e^{-J(\mathcal{M})}, \quad (10)$$

and the constant k_4 is derived from the theorem of total probability applied over all possible models $\mathfrak{M}$, which is integrated by quasi-Monte Carlo using a Sobol sequence with 2^{18} points. The best-fitting model is found by minimizing $J(\mathcal{M})$ instead of maximizing $p(\mathcal{M})$ because

$$\hat{\mathcal{M}} = \underset{\mathcal{M}}{\mathrm{argmax}}\{p(\mathcal{M})|_{\mathcal{C}=\mathcal{C}_i} = k_4 e^{-J(\mathcal{M})}\} = \underset{\mathcal{M}}{\mathrm{argmin}}\{J(\mathcal{M})\}. \quad (11)$$

The probabilistic nature of the reconstruction is partly motivated by the fact that the model itself may not necessarily reproduce the experimental setup, but is just an approximation. It will be shown that if several models are candidates based on different hypotheses about the system, the probabilistic formulation of the inverse problem will be able to provide information to rank the hypotheses. The fundamental idea is that if the model-class (based on the candidate hypothesis) is considered as an uncertain discrete variable, its probability can eventually be extracted as a marginal probability from (6). The probability of each model-class will therefore have the sense of degree of certainty of being true in the sense that the probabilistic conjunction of certainty provided by the experimental measurements and model are coherent.

Let model class $\mathcal{C} \in \mathfrak{C}$ denote an idealized mathematical model hypothesized to simulate the experimental system, whereas model $\mathcal{M}$ denotes the set of physical parameters upon which the model-class depends. Different model classes can be formulated and hypothesized to idealize the experimental system, and each of them can be used to solve the probabilistic inverse problem, yielding different values of model parameters but also physically different sets of parameters. To select among the infinitely many possible model classes that can be defined, a probabilistic criteria can be defined based on their compatibility between prior information about observations $\mathcal{O}$, model parameters $\mathcal{M}$, and model class $\mathcal{C}$, and probabilistic model information [35].

The goal is to find the probability $p(\mathcal{C})$, understood as a measure of plausibility of a model class $\mathcal{C}$ [47]. It can be derived as the marginal probability of the posterior probability $p(\mathcal{O}, \mathcal{M}, \mathcal{C})$ defined in (6),

$$p(\mathcal{C}) = \int_{\mathfrak{O}}\int_{\mathfrak{M}} p(\mathcal{O}, \mathcal{M}, \mathcal{C}) \mathrm{d}\mathcal{M}\mathrm{d}\mathcal{O}$$
$$= k_1 p^0(\mathcal{C})\int_{\mathfrak{O}}\int_{\mathfrak{M}} \frac{p^0(\mathcal{O})p^0(\mathcal{M})p^{\mathrm{m}}(\mathcal{O}\mid\mathcal{M},\mathcal{C})}{\mu(\mathcal{O})} \mathrm{d}\mathcal{M}\mathrm{d}\mathcal{O}. \tag{12}$$

The plausibility of a residue definition given a measurement domain and model class $\mathcal{C}_i$ in the sense of matching between model and experimental observations can be computed by introducing the residue space $\mathcal{R} \in \mathfrak{R}$, and deriving the corresponding marginal probability as

$$p(\mathcal{R}) = \int_{\mathfrak{O}}\int_{\mathfrak{M}} p(\mathcal{R}, \mathcal{O}, \mathcal{M}, \mathcal{C})|_{\mathcal{C}=\mathcal{C}_i} \mathrm{d}\mathcal{M}\mathrm{d}\mathcal{O}$$
$$= \tilde{k}_1 \int_{\mathfrak{O}}\int_{\mathfrak{M}} \frac{p^0(\mathcal{O})p^0(\mathcal{M})p^{\mathrm{m}}(\mathcal{O}\mid\mathcal{R},\mathcal{M},\mathcal{C}_i)}{\mu(\mathcal{O})} \mathrm{d}\mathcal{M}\mathrm{d}\mathcal{O}, \tag{13}$$

where the constant $\tilde{k}_1 = k_1 p^0(\mathcal{C})p^0(\mathcal{R})$. Once $p(\mathcal{C})$ and $p(\mathcal{R})$ are computed for every class and every residue, their values allow ranking of the models according to how compatible they are with the observations. This also allows us to find a correct trade-off between model simplicity and fitting to observations.

The minimization of $p(\mathcal{M})$ for monitoring the evolution of the culture is carried out by two sequential algorithms. When an initial guess is not available, which is the case at the beginning of the process, genetic algorithms are used as a full-range random search technique [48]. Because the change between consecutive measurements of the process is expected to be small, the Broyden–Fletcher–Goldfarb–Shanno (BFGS) algorithm is used as a local search based on Hessian update [49], assisted by finite differentiation and line search.

In the case that the model parameters m are Jeffreys constants [50], they are replaced by unitary logarithmic parameters $\bar{m}$,

$$m_m = m_m^0 e^{\bar{m}\ln(m_m^1/m_m^0)}, \tag{14}$$

which map the dimensional parameters m_m from the preferential range $m_m \in [m_m^0, m_m^1]$ to a nondimensional Jeffreys parameter range $\bar{m} \in [0,1]$. This further stabilizes the search algorithms. In this case, the noninformative distribution $\mu(\mathcal{M})$ can simply be replaced by a constant.

D. NDE-Oriented Signal Processing

This section will provide a suitable representation of the ultrasonic signals, appropriate for tissue reaction process identification. The signals are first preprocessed, by means of a temporal windowing. Then, different parameterization approaches can be applied and the obtained spectral parameters are usually transformed to provide a more uncorrelated and dimensionally reduced representation. As a result of the applied analysis, each signal can be represented by a feature vector containing the analysis

parameters. Finally, some methods are defined to improve the calculation of the discrepancy between the experimental and numerically predicted feature vectors.

1) Preprocessing: After acquisition, the signals have been downsampled at a sampling frequency of 40 MHz, to reduce part of the noise and focus on the frequency range of interest. Second, a normalization with respect to the peak amplitude has been applied, considering that the system must be insensitive to changes in signal amplitude. Finally, the signals have been multiplied by a Hamming window. Because ultrasonic signals are finite by nature, the window is used primarily to weight the signal samples over time, and thus to show off the signal echoes [51].

2) Feature Extraction and Spectral Domain: The proposed methodology includes a nonparametric technique approach that directly estimates the spectrum features from the signal itself, providing a sufficiently accurate representation for many types of signals in many different applications [52], whereas in NDE systems, the pursued information is hidden in a complex signal. Spectral analysis is performed by determining the magnitude spectrum of the detected signals, which is easily obtained by applying the discrete Fourier transform (DFT).

3) Homomorphic Transformations: Among the homomorphic transformations, the basic idea of the cepstrum consists of converting a convolution into a sum [53] and, thus, to obtain a decorrelated representation of the signals. The cepstrum of a discrete signal $s(n)$, whose corresponding spectrum is denoted by $S(\omega)$, is defined as the inverse Fourier transform of the logarithmic spectrum:

$$\hat{c}(n) = \mathfrak{F}^{-1}[\log(S(\omega))] = \frac{1}{2\pi}\int_{-\pi}^{\pi}\log(S(\omega))d\omega. \tag{15}$$

Alternatively, a *real cepstrum* can be obtained by considering the magnitude spectrum $|S(\omega)|$ as

$$c(n) = \frac{1}{2\pi}\int_{-\pi}^{\pi}\log(|S(\omega)|)d\omega. \tag{16}$$

In practice, the real cepstrum can be easily obtained by applying the fast Fourier transform (FFT) as

$$c(n) = \mathrm{IFFT}[\log(|\mathrm{FFT}(s(n))|)], \tag{17}$$

where IFFT denotes the inverse fast Fourier transform. In this case, the real cepstrum is usually called cepstrum FFT. In an algebraic sense, the associated complex cepstrum could be obtained similarly. However, computing the complex cepstrum is usually cumbersome because of the unwrapping of the digital phase. In the cepstral domain, because of the harmonic nature of the ultrasonic signals, the wave components appear as equidistant peaks at higher *quefrencies*, rightly separated by a value that corresponds to the fundamental period of the analyzed signal

echoes [54]. Thus, this cepstral representation allows to decompose the spectrum in its two main characteristics: The spectral envelope and the fine spectrum.

4) Dimensionality Reduction:

It can be useful to restrict the number of cepstral coefficients, by applying a window to rule out lower and/or higher quefrencies. This process is called *liftering*, and is applied as

$$\tilde{c}(n) = c(n)w(n), \tag{18}$$

where $n = 1, \ldots, L$. Several windowing schemes can be directly derived from the rectangular window in the cepstral-domain. This study focuses on *short-pass liftering* [54], which corresponds to a smoothing of the spectrum, preserving its spectral envelope while removing the fine spectrum information. Although it has been less studied, it is interesting to point out that the application of liftering on the complex cepstrum allows observation of the effects of removing quefrencies on the recovered signal in the time-domain. Moreover, applying windows different from the rectangular one allows weighting of the cepstral coefficients depending on their discriminative performance.

E. Discrepancy Between the Experimental and Numerical Feature Vectors

The residue definitions used in the probabilistic inverse problem are generalized to the vectors obtained from the feature extraction. Thus, the residue is defined as a likelihood measure between two feature vectors. The classical residue $\mathbf{r}_0$ has been defined as

$$\mathbf{r}_0 = \mathbf{s^x} - \mathbf{s(p)}, \tag{19}$$

where $\mathbf{s^x}$ and $\mathbf{s(p)}$ denote the vectors obtained from the features extraction, corresponding to the experimental and numerically predicted signals, respectively. Some enhancements are proposed by defining weighted residues. First, a weighted residue is defined which includes the variance of the measurements $\mathbf{s^x}$ over the temporal evolution of the reaction process. Thus, the goodness of fit of the model predictions to the experimental values is assessed with the weighted least squares criterion [55]:

$$\mathbf{r}_1 = \mathbf{s^x}(\mathbf{s^x} - \mathbf{s(p)}). \tag{20}$$

Additionally, a weighted residue is defined which includes the variance of the measurements $\mathbf{s_R^x}$ over the reaction time of the process:

$$\mathbf{r}_2 = \frac{\mathbf{s^x} - \mathbf{s(p)}}{\tilde{\mathbf{s}}_{\mathbf{R}}^{\mathbf{x}}}. \tag{21}$$

Finally, a weighted residue is defined, including both of the aforementioned variances:

$$\mathbf{r}_3 = (\mathbf{s^x} - \mathbf{s(p)}) \frac{\mathbf{s^x}}{\tilde{\mathbf{s}}_{\mathbf{R}}^{\mathbf{x}}}. \tag{22}$$

Note that the variance $\mathbf{s}$ of the coefficients from the experimental signals amounts to a value close to zero when the corresponding signal intensity is low. Thus, a slightly biased variance value $\tilde{\mathbf{s}}$ is used in the residue definitions by making use of the root mean square of the variance $\mathbf{s}$, in order to avoid that the residue tends to infinity:

$$\tilde{\mathbf{s}}^{\mathbf{x}} = \mathbf{s^x} + 0.1 \sqrt{\frac{1}{L} \sum_{n=0}^{L} (\mathbf{s_n^x})^2} \tag{23}$$

Eq. (20)–(22) allow 1) reduction of the uncertainties resulting from measurements noise by assuming statistical independence of the errors and 2) enhancement of parts of the signals that may contain information about the reaction process. In a probabilistic sense, residue definitions that take into account variance information can be understand as a prior knowledge of the measurements' quality and/or evolution of the reaction process. Thus, they may enhance the interpretation of the gelation process.
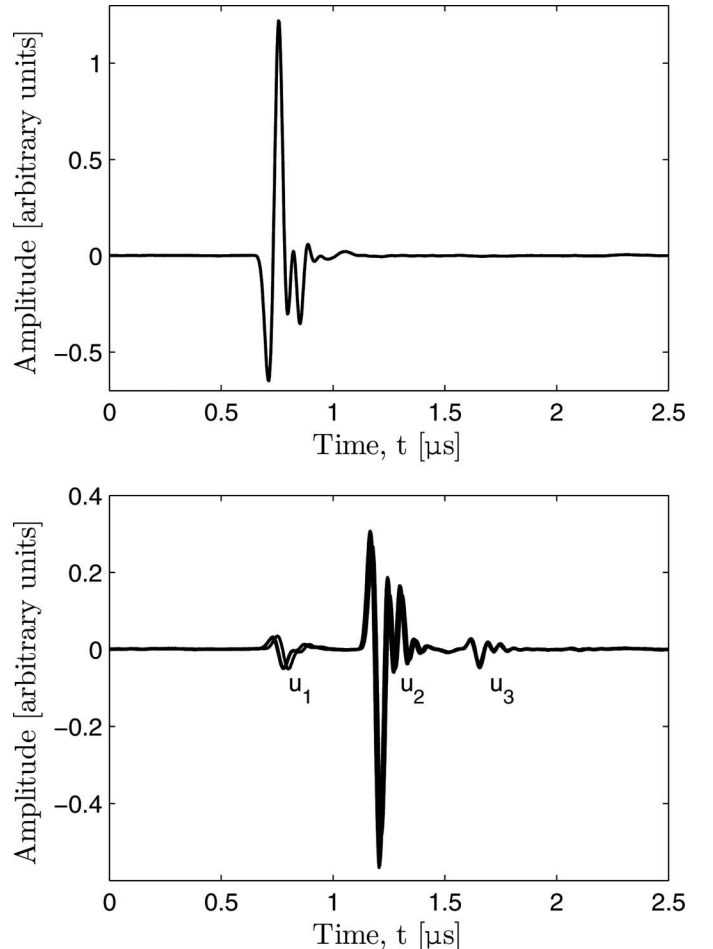

Fig. 2. Signal sample: (top) sequence of signals without specimen, (bottom) signal with specimen registered every 250 s.
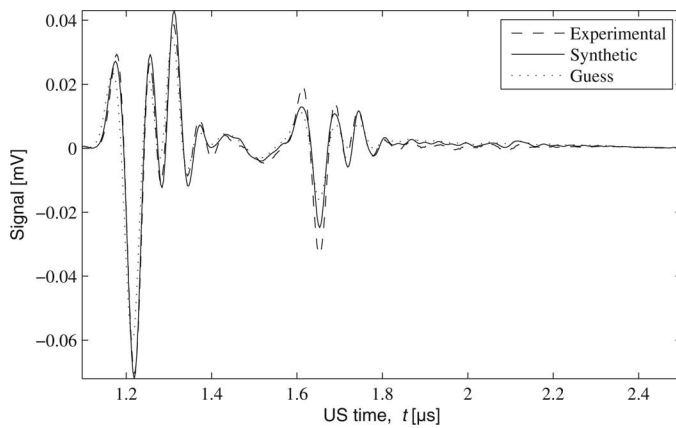
Fig. 3. Example of fitting of experimental and simulated observations: viscous model, time domain, residue $\mathbf{r}_0$.

Fig. 5. Example of fitting of experimental and simulated observations: viscous model, magnitude spectrum, residue $\mathbf{r}_0$.

III. Results

The signals recorded by the ultrasound-monitored Petri dish every 250 s are shown in Fig. 2, with and without the specimen. No clear evolution is detectable by bare visual inspection of the signals. The recorded signals are mainly composed of three different waveforms (simplified paths of Fig. 1), namely, 1) the wave front that propagates only through the PMMA layer (labeled as u_1), 2) a wave that crosses both the PMMA layer and the specimen (labeled as u_2), and 3) a wave echo produced by the former wave after crossing the specimen twice (labeled as u_3).

It is noteworthy that when the specimen is in place, the majority of the excitation signal (registered without specimen for calibration) is transmitted instead of reflected. Because the wavelength in gel is compatible with the layer thickness, the individual echoes generated by the multiple reflections inside the gel layer can be analyzed separately by signal processing.
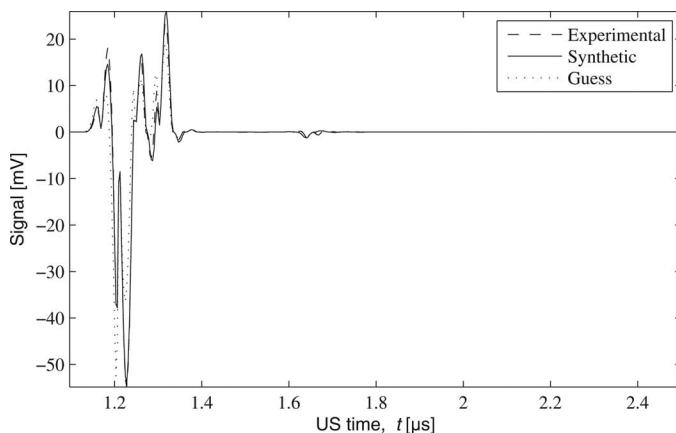
A. Signal Simulation

The transfer matrix formalism is used to generate sample signals, after calibrating the estimated parameters using the inverse problem, for the first signal (initial evolution time). Time-domain signals and magnitude spectra are shown in Figs. 3 to 6 for the viscous model (case 2) at the initial time of the reaction process, respectively. In the lower figures, an analysis window (Hamming) has been applied to the signals and classical and weighted residue definitions are considered, denoted $\mathbf{r}_0$ and $\mathbf{r}_3$, respectively.

A significant ability to simulate the system can be observed visually. The influence of the signal windowing yields the following observations for the magnitude spectrum (Figs. 5 and 6): The envelope, which corresponds to the redundant character of the signal, remains almost unchanged. In contrast, the fine spectrum presents accentuated peakiness because of the enhanced echoes of the time-domain signals. In the time-domain, the classical res-

Fig. 4. Example of fitting of experimental and simulated observations: viscous model, time domain, residue $\mathbf{r}_3$.

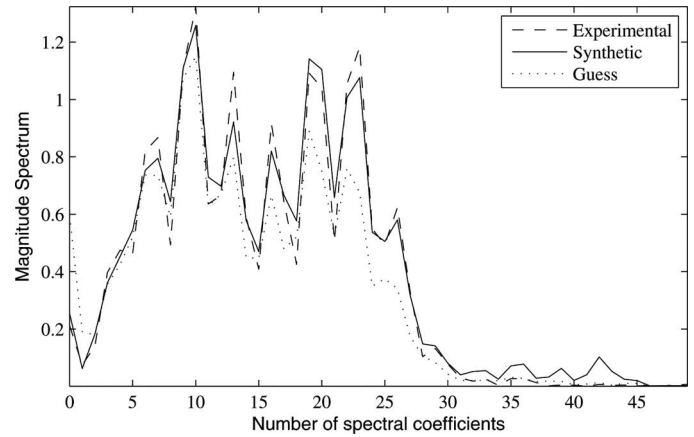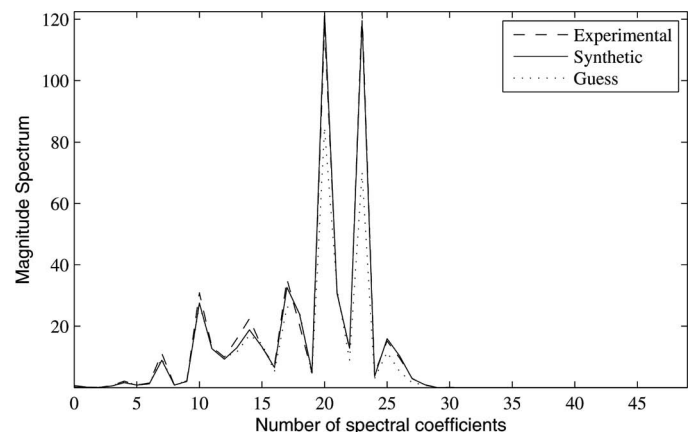Fig. 6. Example of fitting of experimental and simulated observations: viscous model, magnitude spectrum, residue $\mathbf{r}_3$.

Probability Density, $P(m)$ [$\log_{10}$–scale]

Fig. 7. Posterior probability of the model: slice along two parameters, viscous model, time domain, residue $\mathbf{r}_0$.

Probability Density, $P(m)$ [$\log_{10}$–scale]

Fig. 8. Posterior probability of the model: slice along two parameters, viscous model, time domain, residue $\mathbf{r}_3$.

Probability Density, $P(m)$ [$\log_{10}$–scale]

Fig. 9. Posterior probability of the model: slice along two parameters, viscous model, magnitude spectrum, residue $\mathbf{r}_0$.

Probability Density, $P(m)$ [$\log_{10}$–scale]

Fig. 10. Posterior probability of the model: slice along two parameters, viscous model, magnitude spectrum, residue $\mathbf{r}_3$.

Probability Density, $P(m)$ [$\log_{10}$–scale]

Fig. 11. Posterior probability of the model: slice along two parameters, viscous model, real cepstrum, residue $\mathbf{r}_0$.

Probability Density, $P(m)$ [$\log_{10}$–scale]

Fig. 12. Posterior probability of the model: slice along two parameters, viscous model, real cepstrum, residue $\mathbf{r}_3$.

idue $\mathbf{r}_0$ is strongly correlated with the signals themselves (Fig. 3), highlighting higher amplitude where the signals energy is higher. However, the weighted residue $\mathbf{r}_3$ allows removal of some variability resulting from the measurement uncertainties (Fig. 4). Additionally, it enhances the parts of the signal containing information about the reac-

tion process (here, mainly the wave front), while allowing removal of the parts which are invariant to the process evolution (scattering parts). In the frequency domain, the weighted residue allows removal of the frequency range that is insensitive to the reaction process, or is erroneous because of measurement noise. Thus, the resulting mag-

TABLE III. PLAUSIBILITY OF MODEL CLASSES, TIME DOMAIN.

Windowing	Residue	Model class	1	2	3
w_0	$\mathbf{r}_0$	$p(\mathcal{C})$ [%]	31.55	32.39	36.06
		Occam $[-\log_{10}]$	2.24	4.10	1.90
		Certainty $[\log_{10}]$	0.11	0.75	0.37
	$\mathbf{r}_1$	$p(\mathcal{C})$ [%]	33.33	33.33	33.33
		Occam $[-\log_{10}]$	8.11	7.93	11.93
		Certainty $[\log_{10}]$	1.69	1.66	1.97
	$\mathbf{r}_3$	$p(\mathcal{C})$ [%]	15.53	63.10	21.37
		Occam $[-\log_{10}]$	7.34	9.95	14.78
		Certainty $[\log_{10}]$	2.23	2.74	2.97
w_1	$\mathbf{r}_0$	$p(\mathcal{C})$ [%]	32.45	32.99	34.57
		Occam $[-\log_{10}]$	7.14	6.50	7.44
		Certainty $[\log_{10}]$	1.40	1.16	1.02
	$\mathbf{r}_1$	$p(\mathcal{C})$ [%]	33.33	33.33	33.33
		Occam $[-\log_{10}]$	7.93	7.90	13.08
		Certainty $[\log_{10}]$	1.83	1.95	∞
	$\mathbf{r}_3$	$p(\mathcal{C})$ [%]	34.81	31.57	33.62
		Occam $[-\log_{10}]$	4.25	6.17	8.72
		Certainty $[\log_{10}]$	1.39	1.79	1.45

nitude spectra of Fig. 6 show enhanced process information at certain frequencies, in contrast to the magnitude spectrum of Fig. 5.

B. Posterior Probability of the Model

The probability density function is computed for the viscous attenuation model, and some relevant samples issued from the results obtained in the previous section are shown in Figs. 7 to 10. Because the PDF is a multidimensional function, without loss of generality, only a slice along two parameters is represented, namely the bulk modulus of the tissue and the viscous damping coefficient.

The inspection of these plots reveals several local minima—valleys in the probability density function and variations of several orders of magnitude from good to bad model parameters. This implies a bad conditioning of the reconstruction inverse problem and justifies the use of advanced search algorithms such as genetic algorithms. Nonetheless, the use of a weighted residue definition enhances the slope of these local minima, and thus speeds up the convergence of the search algorithm. It is noteworthy that the other attenuation models present similar trends. Additionally, some irrelevant samples resulting from the cepstral analysis are illustrated in Figs. 11 and 12.

The inspection of the plots obtained from the cepstral analysis reveals many local minima that approximately have the same values, leading to an ill-conditioned solution space.

C. Model Class Plausibility

The posterior probability $p(\mathcal{C})$ of every proposed model class $\mathcal{C} \in \mathfrak{C}$ is computed by quasi Monte Carlo integration

TABLE IV. PLAUSIBILITY OF MODEL CLASSES, MAGNITUDE SPECTRUM.

Windowing	Residue	Model class	1	2	3
w_0	$\mathbf{r}_0$	$p(\mathcal{C})$ [%]	29.79	29.39	40.82
		Occam $[-\log_{10}]$	0.09	−0.42	−5.17
		Certainty $[\log_{10}]$	0.40	0.38	0.71
	$\mathbf{r}_1$	$p(\mathcal{C})$ [%]	49.94	50.06	—
		Occam $[-\log_{10}]$	7.71	8.82	—
		Certainty $[\log_{10}]$	1.52	1.63	—
	$\mathbf{r}_3$	$p(\mathcal{C})$ [%]	0.02	56.47	43.51
		Occam $[-\log_{10}]$	4.84	5.88	22.37
		Certainty $[\log_{10}]$	1.93	1.89	4.10
w_1	$\mathbf{r}_0$	$p(\mathcal{C})$ [%]	26.90	26.11	46.99
		Occam $[-\log_{10}]$	2.47	1.82	−8.55
		Certainty $[\log_{10}]$	0.08	0.08	−1.57
	$\mathbf{r}_1$	$p(\mathcal{C})$ [%]	49.98	50.02	—
		Occam $[-\log_{10}]$	8.68	7.81	—
		Certainty $[\log_{10}]$	1.80	1.49	—
	$\mathbf{r}_3$	$p(\mathcal{C})$ [%]	31.98	44.95	23.07
		Occam $[-\log_{10}]$	5.11	4.77	16.15
		Certainty $[\log_{10}]$	1.61	1.54	2.85

TABLE V. PLAUSIBILITY OF MODEL CLASSES, REAL CEPSTRUM.

Windowing	Residue	Model class	1	2	3
w_0	$\mathbf{r}_0$	$p(\mathcal{C})$ [%]	33.33	33.33	33.34
		Occam [$-\log_{10}$]	1.99	2.91	2.67
		Certainty [$\log_{10}$]	0.53	0.45	0.08
	$\mathbf{r}_1$	$p(\mathcal{C})$ [%]	33.33	33.33	33.34
		Occam [$-\log_{10}$]	8.23	8.51	10.95
		Certainty [$\log_{10}$]	2.38	2.42	1.94
	$\mathbf{r}_3$	$p(\mathcal{C})$ [%]	33.33	33.33	33.34
		Occam [$-\log_{10}$]	0.21	2.21	3.28
		Certainty [$\log_{10}$]	0.12	0.31	0.32

using 2^{18} Sobol sampling points. Additionally, the estimation of Occam's factor, as well as the certainty metric $\bar{\sigma}$ are summarized in Tables III, IV, and V for time-domain signals, magnitude spectra, and real cepstra, respectively.

The most plausible model class is shown to be 2, involving K^{tissue}, viscoelastic damping, and temperature and amplitude corrections. It is closely followed by class 1 (hysteretic damping), whereas class 3 does not provide results for all proposed signal processing techniques. The magnitude spectrum computed with weighted residue definitions $\mathbf{r}_1$ and $\mathbf{r}_3$ show significantly higher posterior probability $p(\mathcal{C})$ than the other domains of representation. The real cepstrum provides bad results as well for the posterior probability, which is consistent with the observations in the previous section. This evidence further supports the validity of the probabilistic formulation. Hence, the obtained equiprobable values demonstrate its insensitivity with respect to the selected model classes.

The posterior probability $p(\mathcal{R})$ of every consistent residue definition $\mathcal{R} \in \mathfrak{R}$ is computed according to the posterior probability $p(\mathcal{C})$. Tables VI and VII summarize the obtained values, together with the Occam's factor estimation and certainty metric, for hysteretic and viscous damping, respectively.

The most plausible residue definition appears to be $\mathbf{r}_1$, which involves the inclusion of some prior information on the variance of the measurements over the temporal evolution of the reaction process, when the inverse problem is achieved in the frequency domain. This ranking remains consistent independently of the model class. Signal windowing has a little influence on the improvement of results.

D. Monitoring of Evolution

The evolution of the relevant reconstructed mechanical parameters during the reaction process is shown in Figs. 13 and 14 for the most relevant model class and residue definitions, respectively. The value of the reconstructed bulk modulus at the beginning of the process approximately amounts to 2.385 GPa. Under the hypothesis that the gel layer is already in the gelation zone [38] at the initial process time (for such a thin specimen, the gel starts to gelify almost instantaneously), we suppose that the loss and storage moduli at the initial and end process times approximate those proposed by Wang *et al.* [38], namely $G_0'' = 1200$ Pa, $G_0' = 80$ Pa, and $G_{\text{end}}'' = 1800$ Pa, $G_{\text{end}}' = 140$ Pa, respectively. By making use of the formula [41]

$$c_{\mathrm{p}} = \sqrt{\frac{\left(K + \frac{4}{3}G\right)}{\rho}}, \qquad (24)$$

the wave velocity is found to be 1544 m/s at the initial time of the process. The latter is close to the value given by other authors for similar materials, among them Norisuye *et al.* [37]. Additionally, Norisuye *et al.* suggest that the wave velocity suffers a reduction of around 3%

TABLE VI. PLAUSIBILITY OF RESIDUE DEFINITIONS, TIME-DOMAIN.

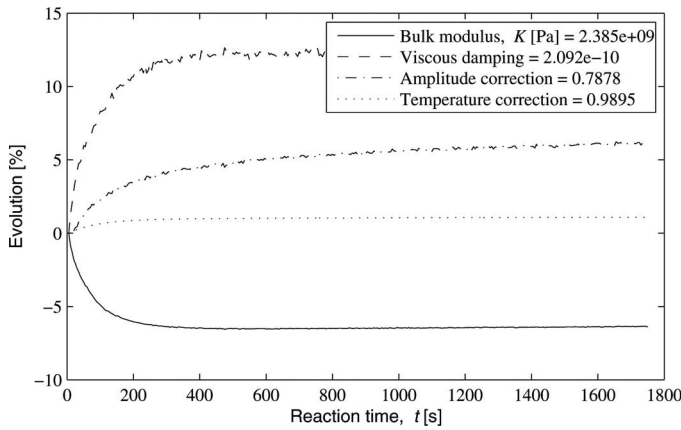| Model	Window	Residue	$\mathbf{r}_0$	$\mathbf{r}_1$	$\mathbf{r}_2$	$\mathbf{r}_3$
1	w_0	$p(\mathcal{R})$ [%]	22.27	26.57	0	0
		Occam	2.24	8.11	−22.96	−7.34
		Certainty	0.11	1.68	−6.30	−2.23
	w_1	$p(\mathcal{R})$ [%]	24.56	26.57	0	0
		Occam	7.14	7.93	−19.54	−4.25
		Certainty	1.40	1.83	−5.40	−1.39
2	w_0	$p(\mathcal{R})$ [%]	22.64	26.31	0	0
		Occam	4.10	7.93	−23.77	−9.95
		Certainty	0.74	1.66	−6.25	−2.74
	w_1	$p(\mathcal{C})$ [%]	24.72	26.31	0	0
		Occam	6.50	7.90	−20.30	−6.17
		Certainty	1.16	1.95	−5.38	−1.79

Fig. 13. Evolution of model parameters during reaction: viscoelastic model, time domain, classical residue, without signal windowing.
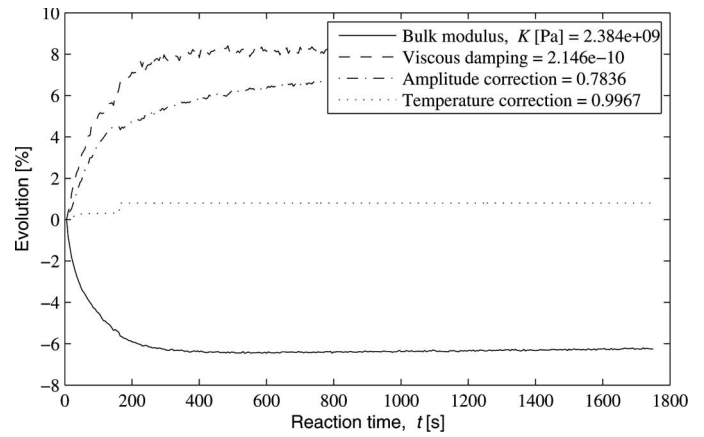

Fig. 14. Evolution of model parameters during reaction: viscoelastic model, magnitude spectrum, weighted residue, signal windowing.

over the reaction process. Thus, the bulk modulus at the end of the process is found to be 2.272 GPa (diminution of 5%), and is in agreement with the value obtained with the proposed formalism.

Some parameter evolutions reconstructed using residues and models with low plausibility (not shown in this paper for brevity) show larger scattering and instabilities, consistent with the results in the two previous subsections. These observations further support the validity of the formulation and conclusions.

IV. Conclusion

A numerical method to determine the elastic and dynamic energy dissipation properties during a gelation process has been developed by combining the solution of a probabilistic inverse problem with signal processing techniques, applying genetic algorithms to minimize a cost function, and using a semi-analytical model of the interaction between ultrasonic waves and tissue.

The proposed model-class and residue selection and their underlying class plausibility have enabled ranking of both the models and the suitable residue definitions according to their compatibility with the observations. The resulting trade-off between model simplicity and fitting to observations has demonstrated that the viscous damp-

ing models, combined with some prior information on the measurements variance over the reaction process evolution, are feasible to characterize the complex evolution of the process.

The reconstructed model parameters highlight the following statements. For the viscoelastic models, the bulk modulus consistently decreases with increasing damping coefficient. Therefore, both parameters may be associated to the same phenomena, but a careful interpretation has not been carried out at this time. The evolution of the model parameters has a stronger slope during the first 200 to 300 s of the reaction process, and remains almost constant afterward. This trend validates the observations done *in situ*, in which the gelation occurred during the first 3 to 5 minutes. Consequently, the proposed methodology demonstrates the capability to discriminate the process during its early solidification phase. For a better understanding of ultrasonic tissue monitoring, *in vitro* studies on real tissue combined with histological studies may be conducted.

TABLE VII. Plausibility of Residue Definitions, Magnitude Spectrum.

Model	Window	Residue	r_0	r_1	r_2	r_3
1	w_0	$p(\mathcal{R})$ [%]	5.87	38.87	0	0
		Occam	0.09	7.71	−14.49	−4.84
		Certainty	−0.40	1.52	−3.98	−1.93
	w_1	$p(\mathcal{R})$ [%]	15.64	39.61	0	0
		Occam	2.47	8.68	−11.81	−5.11
		Certainty	0.08	1.80	−3.40	−1.61
2	w_0	$p(\mathcal{R})$ [%]	5.82	39.12	0	0
		Occam	−0.42	8.82	−14.87	−5.88
		Certainty	−0.38	1.63	−4.00	−1.89
	w_1	$p(\mathcal{C})$ [%]	15.25	39.81	0	0
		Occam	1.82	7.81	−12.02	−4.77
		Certainty	0.08	1.49	−3.35	−1.55

REFERENCES

[1] G. P. Singh and S. Udpa, "The role of digital signal processing in NDT," *NDT Int.*, vol. 19, no. 3, pp. 125–132, 1986.

[2] M. Rodríguez, L. Vergara, and J. Morales, "Real-time prototype for microcracks detection on ceramic materials," in *Proc. IEEE-SP Int. Symp. Time-Frequency and Time-Scale Analysis*, 1996, pp. 469–472.

[3] N. Bilgutay, J. Popovics, S. Popovics, and M. Karaoguz, "Recent developments in concrete nondestructive evaluation," in *Proc. IEEE Int. Conf. Speech Acoustics and Signal Processing*, 2001, vol. 6, pp. 3393–3396.

[4] S. K. Sin and C. H. Chen, "A comparison of deconvolution techniques for the ultrasonic nondestructive evaluation of materials," *IEEE Trans. Image Process.*, vol. 1, no. 1, pp. 3–10, 1992.

[5] S. C. Wooh and C. Wei, "Cepstrum-based deconvolution of ultrasonic pulse-echo signals from laminated composite materials," in *Proc. 12th Engineering Mechanics Conf.*, 1998, pp. 1–4.

[6] K. Harrouche, J. M. Rouvaen, M. Ouaftouh, M. Ourak, and F. Haine, "Signal-processing methods for analysing the structure of carbon-epoxy-resin composite," *Meas. Sci. Technol.*, vol. 11, no. 3, pp. 285–290, 2000.

[7] L. Ghouti and C. H. Chen, "Deconvolution of ultrasonic nondestructive evaluation signals using higher-order statistics," in *Proc. IEEE Int. Conf. Speech Acoustics and Signal Processing*, 1999, vol. 3, pp. 1457–1460.

[8] A. Salazar, R. Miralles, A. Parra, L. Vergara, and J. Gosalbez, "Ultrasonic signal processing for archeological ceramic restoration," in *Proc. IEEE Int. Conf. Acoustics, Speech and Signal Processing*, 2006, pp. 1160–1163.

[9] P. Ramuhalli, J. Kim, L. Udpa, and S. S. Udpa, "Multichannel signal processing methods for ultrasonic nondestructive evaluation," in *Signal Processing Workshop Proc.*, 2002, pp. 229–233.

[10] T. Spencer, M. P. Ramo, D. M. Salter, T. Anderson, P. P. Kearney, G. R. Sutherland, K. A. A. Fox, and W. N. McDicken, "Characterisation of atherosclerotic plaque by spectral analysis of intravascular ultrasound: An in vitro methodology," *Ultrasound Med. Biol.*, vol. 23, no. 2, pp. 191–203, 1997.

[11] U. Scheipers, H. Ermert, H.-J. Sommerfeld, M. Garcia-Schürmann, T. Senge, and S. Philippou, "Ultrasonic multifeature tissue characterization for prostate diagnostics," *Ultrasound Med. Biol.*, vol. 29, no. 8, pp. 1137–1149, 2003.

[12] U. R. Abeyratne and X. Tang, "Ultrasound scatter-spacing based diagnosis of focal diseases of the liver," *Biomed. Signal Process. Control*, vol. 2, no. 1, pp. 9–15, 2007.

[13] S. Maggio, A. Palladini, L. De Marchi, M. Alessandrini, N. Speciale, and G. Masetti, "Predictive deconvolution and hybrid feature selection for computer-aided detection of prostate cancer," *IEEE Trans. Med. Imaging*, vol. 29, no. 2, pp. 455–464, 2010.

[14] S. Siebers, J. Zenk, A. BozzatoE$_\epsilon$, N. Klintworth, H. Iro, and H. Ermert, "Computer aided diagnosis of parotid gland lesions using ultrasonic multi-feature tissue characterization," *Ultrasound Med. Biol.*, vol. 36, no. 9, pp. 1525–1534, 2010.

[15] J. Ophir, I. Céspedes, H. Ponnekanti, Y. Yazdi, and X. Li, "Elastography: A quantitative method for imaging the elasticity of biological tissues," *Ultrason. Imaging*, vol. 13, no. 2, pp. 111–134, 1991.

[16] J. Ophir, S. K. Alam, B. S. Garra, F. Kallel, E. E. Konofagou, T. Krouskop, C. R. B. Merritt, R. Righetti, R. Souchon, S. Srinivasan, and T. Varghese, "Elastography: Imaging the elastic properties of soft tissues with ultrasound," *J. Med. Ultrasonics*, vol. 29, pp. 155–171, 2002.

[17] E. E. Konofagou, J. D'Hooge, and J. Ophir, "Myocardial elastography—A feasibility study in vivo," *Ultrasound Med. Biol.*, vol. 28, no. 4, pp. 475–482, 2002.

[18] J. Bercoff, M. Tanter, and M. Fink, "Supersonic shear imaging: A new technique for soft tissue elasticity mapping," *IEEE Trans. Ultrason. Ferroelectr. Freq. Control*, vol. 51, no. 4, pp. 396–409, 2004.

[19] L. Sandrin, B. Fourquet, J.-M. Hasquenoph, S. Yon, C. Fournier, F. Mal, C. Christidis, M. Ziol, B. Poulet, F. Kazemi, M. Beaugrand, and R. Palau, "Transient elastography: A new noninvasive method for assessment of hepatic fibrosis," *Ultrasound Med. Biol.*, vol. 29, no. 12, pp. 1705–1713, 2003.

[20] A. P. Sarazyan, O. V. Rudenko, S. D. Swanson, J. B. Fowlkes, and S. Y. Emelianov, "Shear wave elasticity imaging: A new ultrasonic technology of medical diagnostics," *Ultrasound Med. Biol.*, vol. 24, no. 9, pp. 1419–1435, 1998.

[21] K. R. Nightingale, M. L. Palmeri, R. W. Nightingale, and G. E. Trahey, "On the feasibility of remote palpation using acoustic radiation force," *J. Acoust. Soc. Am.*, vol. 110, no. 1, pp. 625–634, 2001.

[22] W. F. Walker, F. J. Fernandez, and L. A. Negron, "A method of imaging viscoelastic parameters with acoustic radiation force," *Phys. Med. Biol.*, vol. 45, no. 6, pp. 1437–1447, 2000.

[23] E. A. Barannik, A. Girnyk, V. Tovstiak, A. I. Marusenko, S. Y. Emelianov, and A. P. Sarvazyan, "Doppler ultrasound detection of shear waves remotely induced in tissue phantoms and tissue in vitro," *Ultrasonics*, vol. 40, no. 1–8, pp. 849–852, 2002.

[24] P. P. Delsanto, S. Hirsekorn, V. Agostini, R. Loparco, and A. Koka, "Modeling the propagation of ultrasonic waves in the interface region between two bonded elements," *Ultrasonics*, vol. 40, no. 1–8, pp. 605–610, 2002.

[25] C. Pecorari, "Nonlinear interaction of plane ultrasonic waves with an interface between rough surfaces in contact," *J. Acoust. Soc. Am.*, vol. 113, no. 6, pp. 3065–3072, 2003.

[26] R. A. Guyer, J. TenCate, and P. A. Johnson, "Hysteresis and the dynamic elasticity of consolidated granular materials," *Phys. Rev. Lett.*, vol. 82, no. 16, pp. 3280–3283, 2001.

[27] L. A. Ostrovsky and P. A. Johnson, "Dynamic nonlinear elasticity in geomaterials," *Riv. Nuovo Cim.*, vol. 24, no. 7, pp. 1–46, 2001.

[28] K. E.-A. Van den Abeele, A. Sutin, J. Carmeliet, and P. A. Johnson, "Micro-damage diagnostics using nonlinear elastic wave spectroscopy (NEWS)," *NDT Int.*, vol. 34, no. 4, pp. 239–248, 2001.

[29] M. Muller, D. Mitton, M. Talmant, P. A. Johnson, and P. Laugier, "Nonlinear ultrasound can detect accumulated damage in human bone," *J. Biomech.*, vol. 41, no. 5, pp. 1062–1068, 2008.

[30] G. Renaud, S. Callé, J.-P. Remenieras, and M. Defontaine, "Exploration of trabecular bone nonlinear elasticity using timeof- flight modulation," *IEEE Trans. Ultrason. Ferroelectr. Freq. Control*, vol. 55, no. 7, pp. 1497–1507, 2008.

[31] M. J. Moulton, L. L. Creswell, R. L. Actis, K. W. Myers, M. W. Vannier, B. A. Szab, and M. K. Pasque, "An inverse approach to determining myocardial material properties," *J. Biomech.*, vol. 28, no. 8, pp. 935–948, 1995.

[32] L. Han, A. Noble, and M. Burcher, "The elastic reconstruction of soft tissues," in *Proc. IEEE Int. Symp. Biomedical Imaging*, 2002, pp. 1035–1038.

[33] Z. Guo, S. You, X. Wana, and N. Bicanic, "A FEM-based direct method for material reconstruction inverse problem in soft tissue elastography," *Comput. Struc.*, vol. 88, no. 23–24, pp. 1459–1468, 2010.

[34] K.-V. Yuen, "Recent developments of Bayesian model class selection and applications in civil engineering," *Struct. Saf.*, vol. 32, no. 5, pp. 338–346, 2010.

[35] J. L. Beck and K.-V. Yuen, "Model selection using response measurements: Bayesian probabilistic approach," *J. Eng. Mech.*, vol. 130, no. 2, pp. 192–203, 2004.

[36] S. Cocard, J. F. Tassin, and T. Nicolai, "Dynamical mechanical properties of gelling colloidal disks," *J. Rheol.*, vol. 44, no. 3, pp. 585–594, 2000.

[37] T. Norisuye, A. Strybulevych, M. Scanlon, and J. Page, "Ultrasonic investigation of the gelation process of poly(acrylamide) gels," *Macromol. Symp.*, vol. 242, no. 1, pp. 208–215, 2006.

[38] Y. Z. Wang, X. F. Zhang, and J. X. Zhang, "New insight into kinetics behavior of the structural formation process in agar gelation," *Mech. Eng.*, 2011. Submitted for publication.

[39] R. Ortega, A. Téllez, L. Leija, and A. Vera, "Measurement of ultrasonic properties of muscle and blood biological phantoms," *Phys. Proc.*, vol. 3, no. 1, pp. 627–634, 2010.

[40] L. Gaul, "The influence of damping on waves and vibrations," *Mech. Syst. Signal Process.*, vol. 31, no. 1, pp. 1–30, 1999.

[41] R. Lake, *Viscoelastic Materials*. New York, NY: Cambridge University Press, 2009.

[42] G. Rus, N. Bochud, J. Melchor, M. Alaminos, and A. Campos, "Dispersive model selection and reconstruction for tissue culture ultrasonic monitoring," in *AIP Conf. Proc.*, 2011, vol. 1433, pp. 375–378.

[43] N. M. M. Maia, J. M. M. Silva, and A. M. R. Ribeiro, "On a general model for damping," *J. Sound Vibrat.*, vol. 218, no. 5, pp. 749–767, 1998.

[44] N. Cretu and G. Nita, "Pulse propagation in finite elastic inhomogeneous media," *Comput. Mater. Sci.*, vol. 31, no. 3–4, pp. 329–336, 2004.

[45] A. Tarantola, *Inverse Problem Theory*. Philadelphia, PA: SIAM, 2005.

[46] H. E. Kyburg, *Probability and Inductive Logic*. New York, NY: Macmillan, 1970.

[47] R. T. Cox, *The Algebra of Probable Inference*. Baltimore, MD: Johns Hopkins University Press, 1961.

[48] D. Goldberg, *Genetic Algorithms in Search, Optimization and Machine Learning*, Reading, MA: Addison-Wesley, 1986.

[49] J. E. Dennis and J. J. Moré, "A characterization off superlinear convergence and its application to quasi-Newton methods," *Math. Comput.*, vol. 28, no. 126, pp. 549–560, 1974.

[50] H. Jeffreys, *Theory of Probability*, 3rd ed., Oxford, UK: Clarendon, 1961.

[51] N. Bochud, A. M. Gómez, G. Rus, J. L. Maqueda, and A. M. Peinado, "Robust parametrization for non-destructive evaluation of composites using ultrasonic signals," in *Proc. IEEE Int. Conf. Acoustics, Speech and Signal Processing*, 2011, pp. 1789–1792.

[52] M. H. Hayes. *Statistical Digital Signal Processing and Modeling*. New York, NY: Wiley, 1996.

[53] J. S. Lim and A. V. Oppenheim, *Advanced Topics in Signal Processing*. Englewood Cliffs, NJ: Prentice Hall, 1988.

[54] D. G. Childers, D. P. Skinner, and R. C. Kemerait, "The cepstrum: A guide to processing," *Proc. IEEE*, vol. 65, no. 10, pp. 1428–1443, 1977.

[55] S. C. Constable, R. L. Parker, and C. G. Constable, "Occam's inversion: A practical algorithm for generating smooth models from electromagnetic sounding data," *Geophysics*, vol. 52, no. 3, pp. 289–300, 1987.

Guillermo Rus started his research on computational mechanics at the University of Granada (UGR) in 1995, where he defended his Ph.D. thesis on Numerical methods for nondestructive identification of defects in 2001, providing defect search algorithms and sensitivity computation with boundary elements. He applied these experimentally at the NDE Lab at MIT (Cambridge, MA) as a Fulbright Postdoctoral Fellow, rendering novel robust quantitative approaches to ultrasonics and impact testing. He started up the NDE Lab at the UGR (http://www.ugr.es/~grus) in 2003 to focus on bioengineering applications, such as bone implant debonding in collaboration with University College London, bone quality diagnosis with ultrasound with Université Paris VI, and biomaterials characterization with the Nanomaterials Technology Laboratory and Institute of Bioengineering, Alicante. He is also transferring this diagnosis technology to civil engineering for monitoring the structural health of advanced materials such as CFRP, in collaboration with Andong National University, Korea. Rus was tenured as an associate professor in 2009 at UGR, and is the author of 20 SCI papers and 7 books, in addition to 40 international conference contributions and 11 invited presentations. His research career was awarded the Juan Carlos Simo prize for young researchers (Spain, 2007), the Honorary Fellowship of the Wessex Institute of Technology (UK, 2005), Fulbright Fellowship (USA, 2002) and the Excellence Ph.D. award (Granada, 2001).

Nicolas Bochud received a master's degree in mechanical engineering from the Swiss Federal Institute of Technology (ETH), Zurich, in 2008, and a master's degree in information technology from the University of Granada, in 2010. He is currently pursuing his Ph.D. degree in the Department of Structural Mechanics of the University of Granada, focusing on the identification of pathologies in advanced materials and biomaterials using ultrasonics. His research field includes nondestructive evaluation, signal processing, and nonlinear ultrasound.